11TH INTERNATIONAL SYMPOSIUM ON PARTICLE IMAGE VELOCIMETRY – PIV15
Santa Barbara, California, September 14-16, 2015

SAND2015-6915C

Time-Resolved PIV in a Shock Tube using a Pulse-Burst Laser

Justin Wagner, Steven Beresh, Edward DeMauro, Katya Casper, Brian Pruett, Paul Farias

Department of Engineering Sciences, Sandia National Laboratories, Albuquerque, New Mexico, 87185
jwagner@sandia.gov

ABSTRACT

Time-resolved particle image velocimetry (TR-PIV) measurements are made in a shock tube using a pulse-burst laser. Two transient flowfields are investigated including the baseline flow in the empty shock tube and the wake growth downstream of a cylinder spanning the width of the test section. Boundary layer growth is observed following the passage of the incident shock in the baseline flow, while the core flow velocity increases with time. Comparison of this measured core flow acceleration to that predicted using classical unsteady boundary layer growth models shows good agreement in some instances. As a result of wall boundary layers, a significant amount of spatial non-uniformity remains in the flow following the passage of the end-wall reflected shock. In the transient wake growth measurements, the wake downstream of the cylinder is symmetric immediately following the passage of the incident shock. At later times, the wake transitions to von a Kármán vortex street. The TR-PIV data are bandpass filtered about the vortex shedding frequency and its harmonics to reveal additional details on the transient wake growth.

INTRODUCTION

Previous PIV measurements in shock tubes have typically been limited to low repetition rates allowing for only one realization to be obtained in the millisecond test times of a shock tube [1]. Recent advances and the commercialization of the pulse-burst laser along with gains in high-speed camera technology, however, have made time-resolved PIV in high-speed flows a feasible and attractive option [2]. Towards this end, time-resolved PIV measurements in Sandia's Multiphase Shock Tube (MST) using a pulse-burst laser are demonstrated here for two transient flow fields.

The transients of the flow in the baseline (empty) shock tube are first presented. Following the passage of the incident shock wave, the flow conditions in a shock tube vary due to unsteady boundary layer effects [2-7]. Weak waves are produced by the boundary layer, which result non-uniformities in the core flow of the shock tube. Mirels and Braun [7] developed a model based on perturbation methods to estimate this influence of turbulent boundary layer growth on the time variation of fluid properties, including core flow velocity. In shock tube studies attempting to quantify particle drag [7-12], it is important that temporal variations in core flow velocity be assessed if accurate measurements of the drag coefficient C_d are to be obtained [12]. However, there are very little data to do so. This work seeks to address this shortcoming through time-resolved velocity measurements of the core flow, which are compared to the predictions of Mirels and Braun [7]. The baseline data are also used to quantify boundary layer growth and shock-induced separation associated with the end wall reflected shock as it propagates back into the test section.

Measurements on the shock-induced transient growth of a wake downstream of a circular cylinder are then presented. The transient wake growth of impulsively started bodies has been studied in several low-speed experiments using liquid tow tanks [13-15] and impulsively started contraptions in air [16]. On the other hand, transient wake formation in a high-speed, impulsive facility like a shock tube has received less attention. Previous work has visualized the wake formation and quantified vortex motion in a shock tube using interferometry [17]. The current study uses time-resolved PIV to quantify the transient phenomena associated with an impulsively started cylinder.

EXPERIMENTAL SETUP

Multiphase Shock Tube

All experiments were conducted in the MST, which has been described in detail in previous work [18] and is only briefly summarized here. The MST consisted of a circular driver pipe having a diameter of 89 mm and a length of 2.1 m. The

This work is supported by Sandia National Laboratories and the United States Department of Energy. Sandia National Laboratories is a multi-program laboratory managed and operated by Sandia Corporation, a wholly owned subsidiary of Lockheed Martin Corporation, for the U.S. Department of Energy's National Nuclear Security Administration under contract DE-AC04-94AL85000.

driven section is formed from square tubing having an inner width of 79 mm. The driven gas was ambient air at an initial temperature of about 300 K and an initial atmospheric pressure of about 84.1 kPa. A modular design of the driven section allowed for the location of the test section and the length of the shock tube to be varied (Fig. 1). Experiments were conducted with a 5.2 m long driven section. Additionally, separate sets of experiments were performed where the driven section was lengthened to 5.6 m by adding a driven section to the shock tube to delay the arrival of the reflected shock at the section.

Incident shock waves were generated using three different shock tube configurations. The first used the burst disk holder section (Fig. 1), which was loaded with a single burst disk serving as the diaphragm. The inner diameter of the burst disk holder is the same as the driver section. As a result, there is an abrupt area change as the incident shock travels from the burst disk holder through the driven section. Previous experiments have shown the incident shock to be planar upon arrival at the test section, however. The MST was run in the configuration of Fig. 1 with burst disks having rupture pressures of 480, 2760, and 4140 kPa. This produced nominal incident shock Mach numbers M_s of 1.45, 1.64, and 1.91, respectively. As detailed in [18], in this configuration the MST relies on a slow fill process to rupture the diaphragm. As a result, the jitter in diaphragm rupture time is several seconds, making it difficult to time the burst of the disk to instrumentation such as a laser.

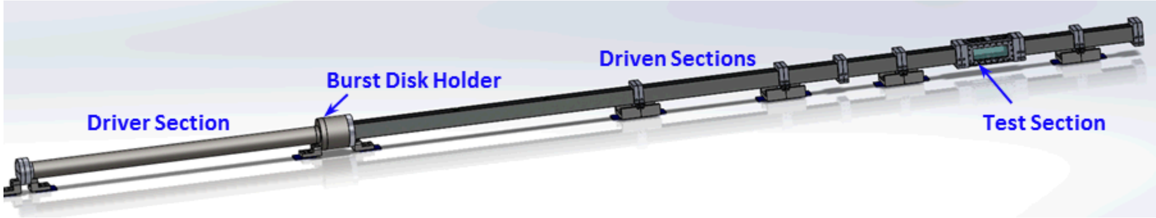

Fig. 1 MST in single-diaphragm configuration and with a 5.6 m long driven section.

To improve timing, a double-diaphragm capability was recently added to the MST. As shown in Fig. 2a, the double-diaphragm section consisted of an additional circular section with small internal volume in between the driver and driven sections. A burst disk was installed at each end of this section, with the upstream disk having a higher burst pressure than the downstream disk, which has a burst pressure of about 380 kPa. Prior to a double-diaphragm experiment, the volume in between the burst disks was pressurized to a value dependent on the desired shock Mach number (and the rupture pressure of the upstream disk required). To fire the shock tube, the small volume in between the driver and driven sections was rapidly evacuated to vacuum through a tube with diameter of 38 mm, connected to a fast acting valve having the same diameter. The valve had an opening time of only a few ms. As a result of the fast acting valve and the small evacuation volume between the disks, the shock tube could be operated in the double-diaphragm configuration with a jitter of less than 10 ms on the disk rupture time.

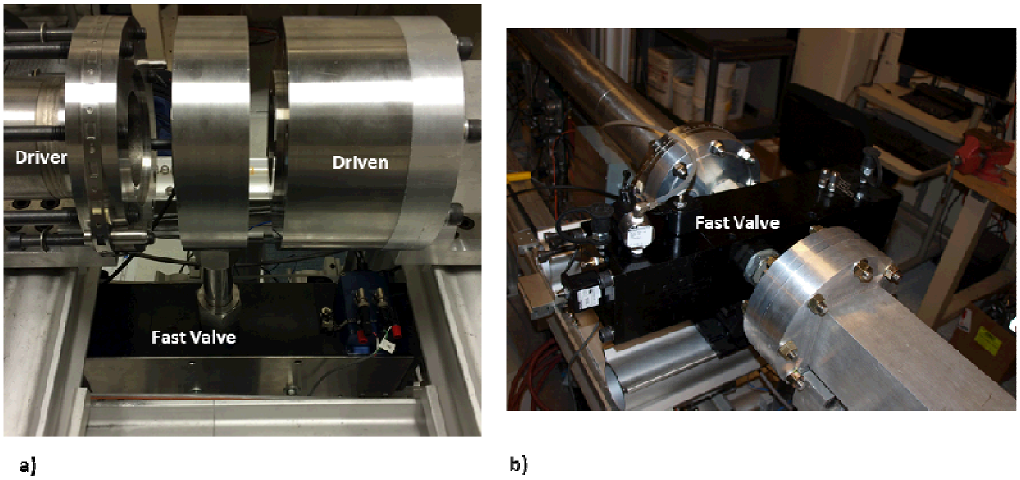

Fig. 2 Additional configurations to create the incident shock: a) double-diaphragm, and b) fast-valve.

A third method to produce the incident shock wave replaced burst disks entirely with a Dynamics Systems Research (model 183-1.5-2000) fast acting valve. This 'fast-valve' configuration is shown in Fig. 2b, where the valve is seen placed between the driver and driven sections. The advantages of using the fast-valve configuration include faster turnaround time between runs and a lower operation lower cost since burst disks are no longer required. The valve diameter was half the width of the driven section. As a result, when the valve opened, the shock wave leaving the valve expanded to fill the width of the driven section as it propagated downstream. Schlieren and PIV measurements in the test section indicated the shock to be planar. However, because of the 38 mm valve diameter, the driver pressure to produce equivalent M_s at the test section was significantly higher in this configuration than in the burst disk configurations. For instance, a disk with nominal burst pressure of 480 kPa resulted in a shock Mach number of 1.45 with the burst disk configurations. To achieve this same M_s in the fast-valve configuration required a driver pressure of 2760 kPa. Comparisons at $M_s = 1.45$ between the burst disk and fast-valve configurations are made herein. Moreover, the fast-valve configuration was operated at driver pressures of 2070, 1380, and 690 kPa, resulting in shock Mach numbers of 1.39, 1.32, and 1.22, respectively.

Pulse-Burst PIV

A Quasi-Modo (Spectral Energies, LLC) burst-mode laser provided the light source for the PIV measurements. The laser design is based on master oscillator power amplifier architecture and is similar to previously reported pulse-burst lasers [19, 20]. The laser is capable of repetition rates of 5 kHz – 500 kHz, which produce maximum pulse energies of 500 mJ and 20 mJ, respectively. In order to produce such large energies at high repetition rates, the laser has a low duty cycle, meaning that it can fire only once every eight seconds at a maximum burst duration of 10.2 ms. Such duration, however, is longer than the typical test time in the MST making it an ideal tool to maximize repetition rate and pulse energy in a transient facility. For PIV, the laser can be operated in a doublet mode where the inter-pulse separation time Δt can be adjusted. In other words, the laser outputs two high-repetition-rate bursts separated by a user defined Δt. In the current work, the pulse separation time was varied from 2 μs – 4 μs according to the flow conditions. The laser was operated at a repetition rate of 50 kHz with energy of about 20 mJ per pulse. Typical sheet-forming optics were used to shape the laser beam into a 1.5-mm thick laser sheet, which was aligned parallel to the streamwise direction. The laser sheet entered the test section through a fused-silica window in the test section ceiling and was located at the spanwise center of the test section. The laser was triggered using a pressure sensor roughly 350 mm upstream of the test section.

Seed particles were produced using a TSI six-jet atomizer and entered the shock tube about 0.5 m downstream of the diaphragm through a remotely actuated solenoid and a duct having a diameter of 25 mm. An additional high-pressure solenoid and duct were installed at the end of the driven section to provide an exit flow path for the particles in order to adjust seed density. The exit duct was connected to a lab fume hood exhaust to produce a slight pressure drop to allow flow through the shock tube. Prior to an experiment, the high-pressure solenoid valves were opened to fill the tube with particles. The valves were closed before generation of the incident shock.

Two Photron (SA-Z) cameras, fitted with 100-mm focal length lenses, were placed on opposite sides of the test section to view adjacent image fields with a small overlap (Fig. 3). The combined field-of-view was about 40 mm × 35 mm. Each camera was operated at 100 kHz to frame-straddle the 50 kHz doublets and the pixel resolution of each camera was 680 × 340. The PIV images were processed with the LaVision (Davis 8.2) software package to a final interrogation window of 24 × 24 pixels^2 (1.8 × 1.8 mm^2) at a 50% overlap. The cameras were triggered off of the same pressure sensor as the laser and were synchronized using a LaVision high-speed controller and Stanford Research Systems (model DG 645) digital delay generator.

The pulse-burst PIV system was used to measure two transient flowfields. The first flow was the baseline flow in the empty shock tube. In this case, the cameras were positioned to view a region through large BK7 windows that included the lower wall of the shock tube up through the wall-normal centerline of the test section. The second set of measurements quantified the transient wake growth downstream of a cylinder. The cylinder had a diameter d of 14 mm and it spanned the entire test section width. In this case, the cameras viewed the flow through acrylic windows through which the cylinder was bolted in place (Fig. 3). The shock tube was run in the fast-valve configuration in the cylinder experiments to obtain a larger dataset than would have been possible using the burst disks.

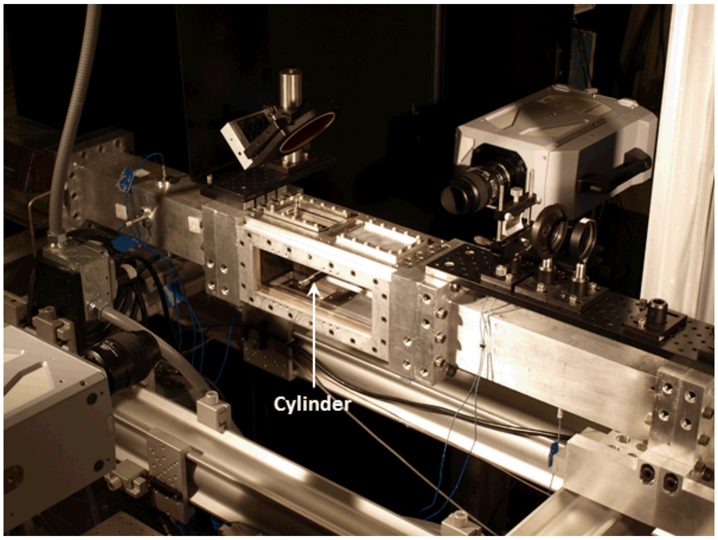

Fig. 3 Photo showing the test section with the full-span cylinder installed and the high-speed cameras.

RESULTS

Baseline Flow in Empty Shock Tube

The baseline flow during an experiment with an incident shock Mach number of 1.45 is shown in Fig. 4. The experiment used the double-diaphragm configuration. Streamwise velocity contours with velocity vectors overlaid are displayed and the flow is left-to-right as is the case with all figures herein. In the baseline data, time is defined to begin when the incident shock is at the center of the vector field and $y = 0$ is defined to be the lower wall. At $t = -20$ µs (Fig. 4a), the incident shock has entered the field-of-view. The shock has an apparent streamwise thickness owing to the finite response time of the particles, a result which is quantified subsequently. As time proceeds to 1800 µs (Fig. 4b), low velocity fluid appears near the lower wall as the boundary layer grows. As time progresses to 3400 µs (Fig. 4c), and then to 4880 µs (Fig. 4d), the boundary layer continues to grow in a turbulent fashion. Over roughly the first 5 ms, the core velocity increases by about 15% from 215 m/s to about 245 m/s. By $t = 5060$ µs (Fig. 4e), the reflected shock from the end wall appears near $x = 25$ mm. The reflected shock does not bring the flow to rest. Rather the streamwise velocity remains around 30 m/s – 50 m/s. At 5400 µs (Fig. 4f) the velocity in the wall-normal center of the shock tube remains elevated around 65 m/s and a large region of reverse flow exists near the floor having minimum velocity of about -30 m/s.

Baseline results corresponding to a double-diaphragm test at $M_s = 1.64$ are shown in Fig. 5. The incident shock induces a flow velocity in its wake of 295 m/s (Fig. 5a). As time increases from 1820 µs (Fig. 5b) to 4720 µs (Fig. 5d) growth of a turbulent boundary layer along lower wall is once again evident. The core flow velocity increases by about 20% over the first 4.7 ms of the experiment. At 4900 µs (Fig. 5e) the reflected shock has propagated upstream through most of the vector field. Like in Fig. 4, the reflected shock does not bring the flow to rest. On the contrary, a remaining core flow velocity of roughly 100 m/s is evident. Flow separation along the lower wall begins about 20 mm downstream of the reflected shock. A region of reverse flow along the floor continues to persist with a minimum velocity of about -90 m/s (Fig. 5f).

The measured velocities across the $M_s = 1.45$ and $M_s = 1.64$ incident shock waves are shown in Fig. 6. The plots were produced by averaging over the vertical extent of the vector fields shown in Fig. 4a and Fig. 5a. At Mach 1.45 it takes about 2.4 mm for the streamwise velocity to reach 63% of the maximum and at Mach 1.64 this relaxation distance is about 2.7 mm. Using these relaxation distances across the normal shock and a shock-fixed reference frame gives a particle response time τ_p of about 5.9 µs in both instances [21]. Under the assumption of Stokes drag, the particle diameter then computes to be about 1.6 µm. Analysis of $M_s = 1.91$ data yielded a particle size. The Stokes number for typical turbulent boundary layer eddies, such as those in Fig. 4 and Fig. 5, ranges from about 0.05 – 0.15. Therefore, the PIV seed particles are expected to faithfully track velocity fluctuations during boundary layer growth [22].

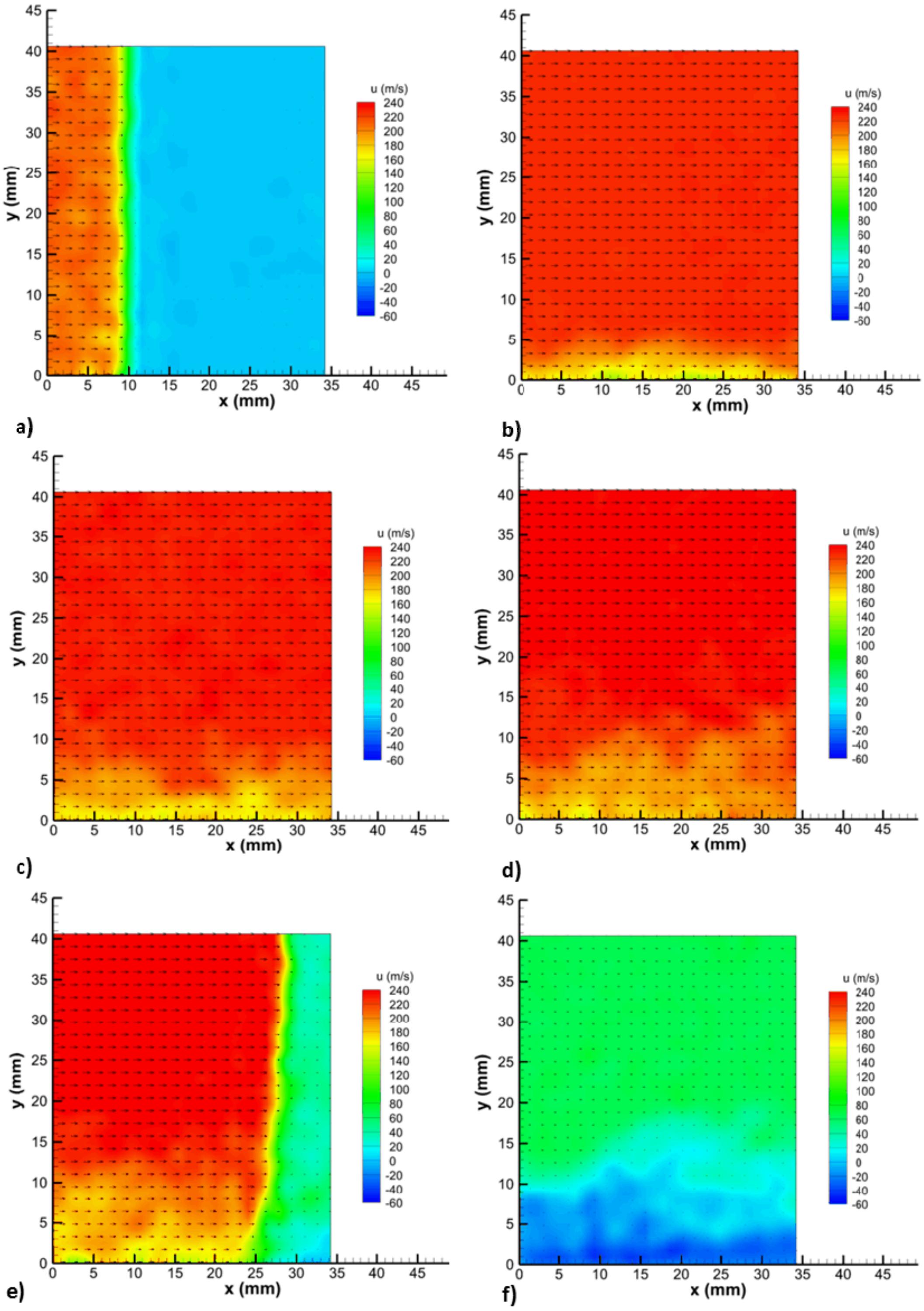

Fig. 4 Streamwise velocity contours and velocity vectors during a baseline run with M_s = 1.45 at times: a) *t* = -20 µs, b) *t* = 1800 µs, c) *t* = 3400 µs, d) *t* = 4880 µs, e) *t* = 5060 µs, and f) *t* = 5400 µs. Vectors are subsampled by a factor of two in *x* and *y*.

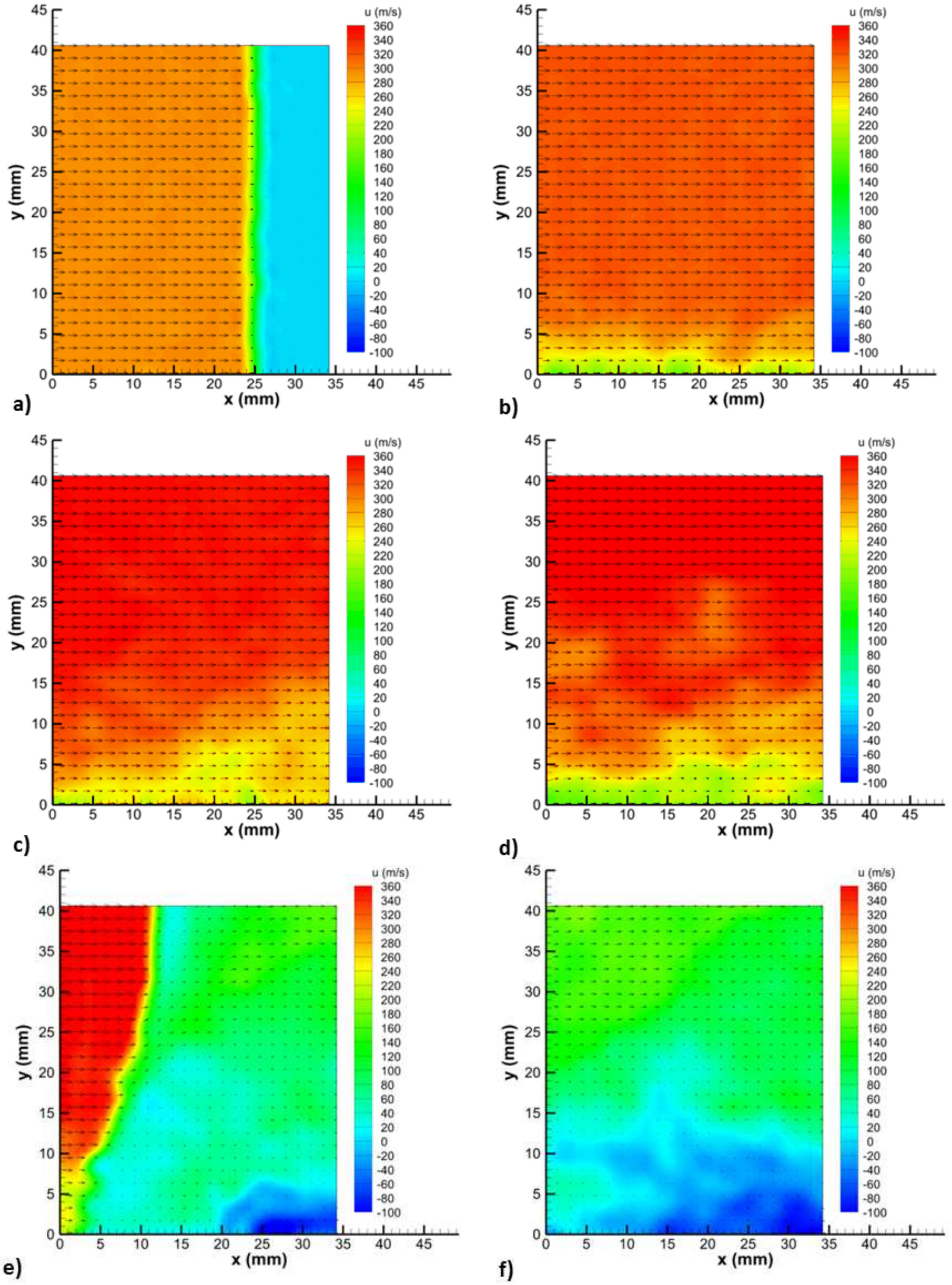

Fig. 5 Streamwise velocity contours and velocity vectors during a baseline run with $M_s = 1.64$ at times: a) $t = 20$ μs, b) $t = 1820$ μs, c) $t = 3420$ μs, d) $t = 4720$ μs, e) $t = 4900$ μs, and f) $t = 5420$ μs. Vectors are subsampled by a factor of two in x and y.

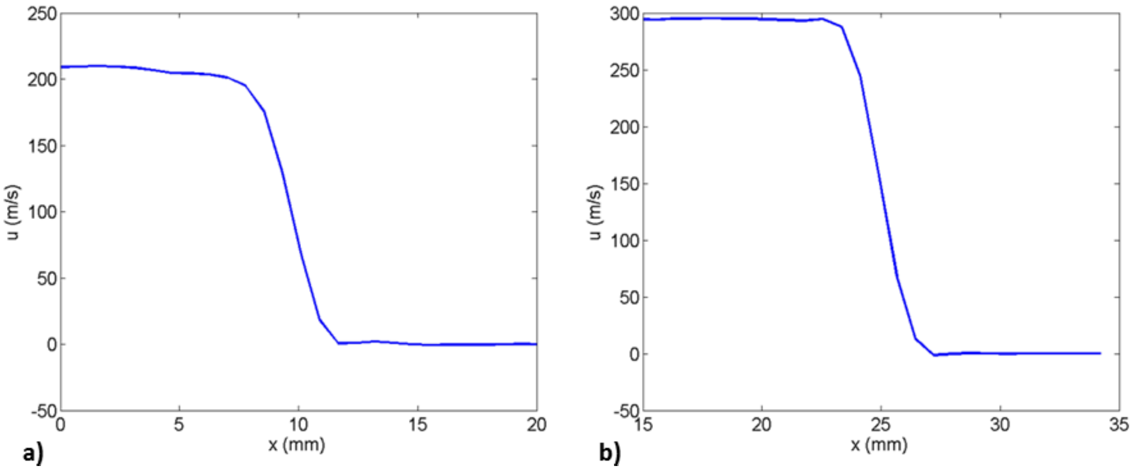

Fig. 6 Streamwise particle velocity across the incident shock at: a) $M_s = 1.45$, and b) $M_s = 1.64$.

Streamwise velocity profiles at five different times during the Mach 1.45 baseline flow are shown in Fig. 7. The profiles were obtained by averaging over the entire streamwise extent of the vector fields and by averaging over five different $M_s = 1.45$ experiments. The non-normalized profiles in Fig. 7 demonstrate an increasing core flow velocity. To quantify boundary layer thickness, velocity profiles were normalized by the core flow velocity U_2 and are plotted against the wall-normal coordinate normalized by the test section height (and width) *D*. The core flow velocity was obtained by averaging over the streamwise extent of the vector fields at a height of 39.6 mm, which corresponds to the wall-normal center of the test section. The normalized plots show that the 99% boundary layer thickness δ increases from about 4% of the test section height at 0.2 ms to about 15% at 3.4 ms. Over this time range, the velocity measured near $y = 0$ decreases from about $0.85U_2$ to about $0.50\ U_2$.

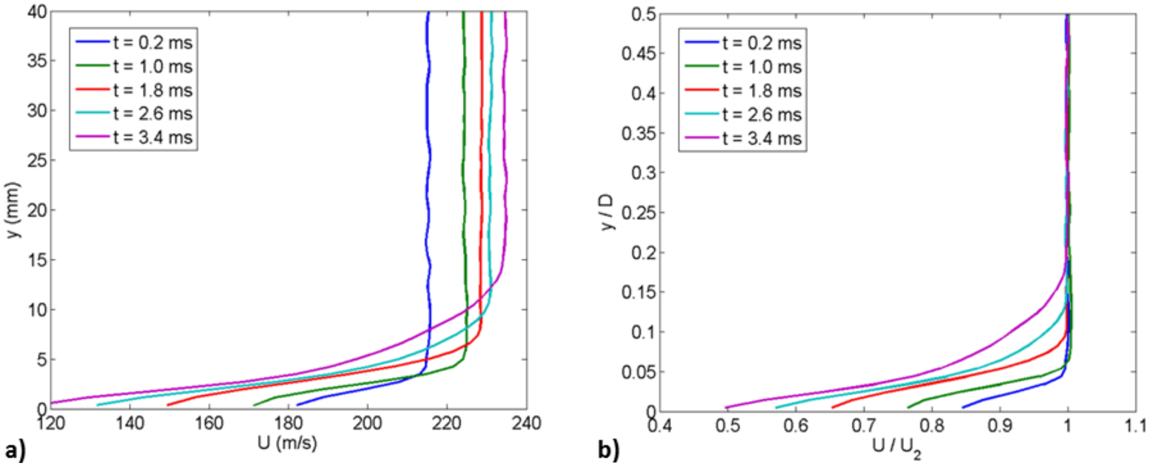

Fig. 7 Streamwise velocity profiles following the passage of the $M_s = 1.45$ incident shock: a) non-normalized, and b) normalized.

Boundary layer growth is quantified further in Fig. 8 for the incident shock Mach numbers of 1.45 and 1.64. The boundary layer growth plots are the average of five different experiments and the error bars correspond to precision uncertainty on this mean based on student-t theory. Non-normalized curves are given in Fig. 8a and normalized data are presented in Fig. 8b. Non-dimensional time t^* is time multiplied by W_s / D, where W_s is the incident shock velocity. The $M_s = 1.45$ data suggest a parabolic growth of δ with time. The $M_s = 1.64$ plot, on the other hand, appears noisier and it is therefore unclear whether a similar parabolic behavior occurs. In either event, the normalized profiles in Fig. 8b show the boundary layer thickness reaches about 45% of the test section height with $M_s = 1.64$, and about 30% of D at $M_s = 1.45$.

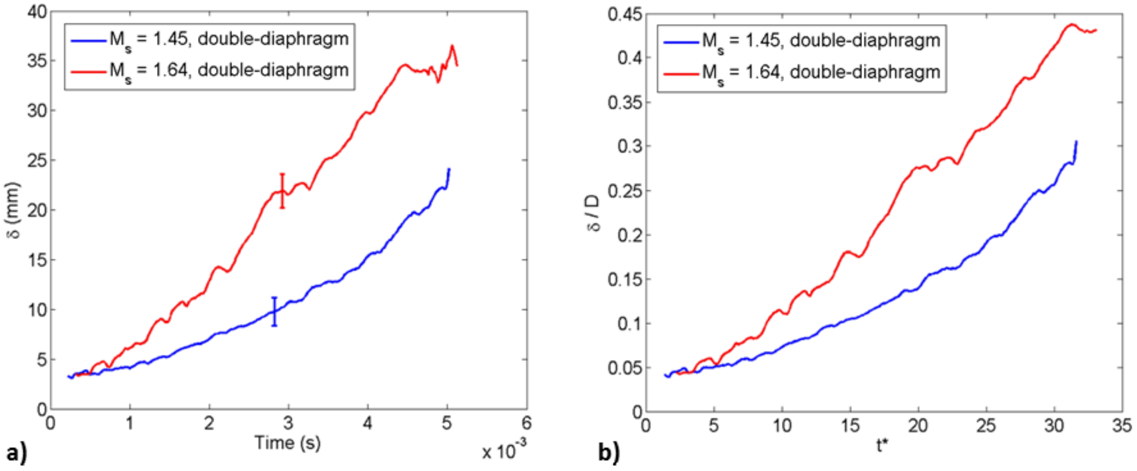

Fig. 8 Boundary layer thickness as a function of time following the passage of the incident shock: a) non-normalized, and b) normalized.

The streamwise core flow velocity normalized by the initial shock-induced velocity $U_{2,0}$ is presented in Fig. 9 as a function of time. The plots are averages based on four runs and the precision uncertainty on these averages is typically less than 2%. The predicted core flow velocity using the model of Mirels and Braun [7] is also shown in the figure. A comparison between the double-diaphragm and single-diaphragm configurations is made at $M_s = 1.45$ (Fig. 9a) and at $M_s = 1.64$ (Fig. 9b). At $M_s = 1.45$, the single- and double-diaphragm data are similar up until about 0.6 ms, but afterwards, the single-diaphragm velocity accelerates at a significantly greater rate than the double-diaphragm. For nearly the entire experiment, the double-diaphragm plot is in good agreement with model of Mirels and Braun. The data at $M_s = 1.64$ tell a similar story. Up until about 0.8 ms, the single-diaphragm and double-diaphragm velocities are similar and they are in good agreement with the model. After 0.8 ms, the single-diaphragm curve once again diverges from that of the double-diaphragm. The double-diaphragm data continue to be well predicted by Mirels and Braun until about 1.6 ms, when a more rapid acceleration is observed. With $M_s = 1.91$ (Fig. 9c), the measured and predicted core flow velocities are in good agreement, particularly for times up until about 1.5 ms. Finally, comparisons of the single-diaphragm configuration at all three Mach numbers in normalized form are shown in Fig. 9d, where for t^* less than 17, the core flow acceleration is seen to be less than 14%.

Several additional observations can be gathered from Fig. 9. First, the core flow acceleration tends to be lower in the double-diaphragm configuration than in the single. This may indicate that the burst disks rupture more cleanly and rapidly in the double-diaphragm case. This is perhaps because in the double-diaphragm case, the process of evacuating the small volume between burst disks is much more rapid than the fill process in single-diaphragm configuration (ms versus s timescales). In either event, such information would be lost without direct measurement of the velocity. Figure 6 also shows that the Mirels and Braun model does a reasonable job predicting core flow accelerations at $M_s = 1.91$ (Fig. 9c) and in the double-diaphragm cases at $M_s = 1.45$ (Fig. 9a) and $M_s = 1.64$ (Fig. 9b). In general, the Mirels and Braun model tends to either agree with the measurements or under predict the core flow acceleration. Thus, the model tends to give a best case estimate for the undesirable core flow acceleration.

The arrival of the reflected shock is seen with the rapid decrease in velocity in Fig. 9. In each case the core flow velocity is significantly greater than zero as would be predicted by ideal theory. The presence of wall boundary layers explains this deviation. The post-reflected shock velocities are greater in the cases with longer test times (and therefore thicker wall boundary layers). For instance, at Mach 1.45, the double-diaphragm post-reflected shock velocities are about 30% of $U_{2,0}$ compared to 20% in the shorter test times of the single-diaphragm data. A similar trend is also seen at $M_s = 1.64$. Moreover, the normalized velocity following the arrival of the reflected shock increases with the shock Mach number.

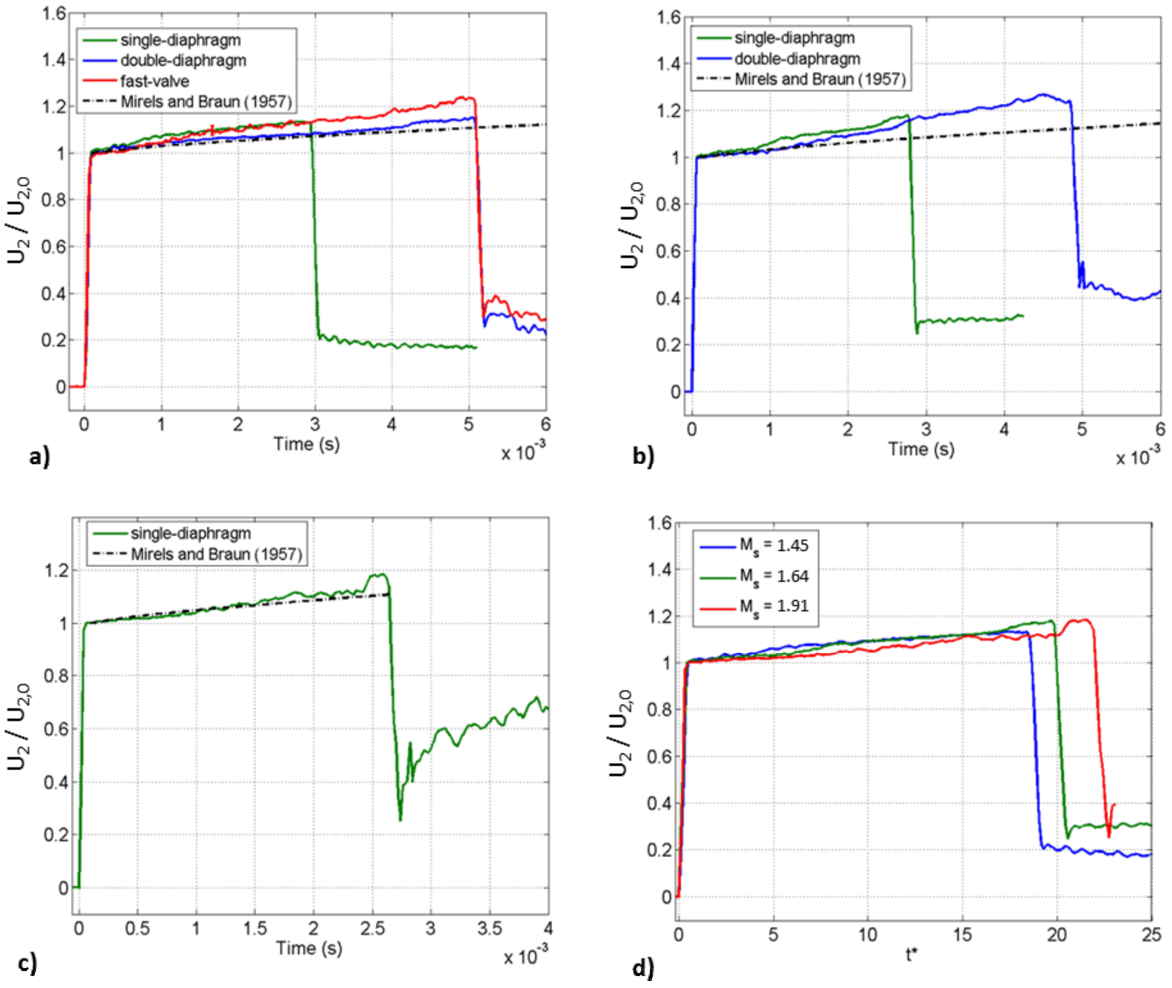

Fig. 9 Core flow velocity as a function of time: a) $M_s = 1.45$, b) $M_s = 1.64$, c) $M_s = 1.91$, d) comparison of core flow acceleration at three Mach numbers as a function of t^*.

Collectively, the results in Fig. 4 - Fig. 9 highlight the importance of time-resolved velocity measurements in baseline shock tube flows. Unsteady boundary layer growth will lead to an acceleration of the core flow. If the aim of an experiment is to measure C_d [8-12, e.g.], an error of 10% in shock-induced velocity will lead to an error of 21% in C_d. Such effects can be corrected for by estimating boundary layer growth effects [12], but small configurational changes, such as between the single- and double diaphragm herein, can lead to large variations in the behavior of the flow following the incident shock that may not be obvious without velocity data. Moreover, many shock tube experiments rely on the post-reflected shock flow for combustion chemistry measurements [23, 24]. Time-resolved, full-field measurements of the velocity field could help interpretation of these measurements by quantifying the effects of boundary layer growth and shock-induced separation on ignition.

Core flow velocity time traces obtained with the fast-valve configuration are displayed in Fig. 10 for four different driver pressures and incident shock Mach numbers. At $M_s = 1.22$, the shock-induced velocity remains close to its initial value of about 110 m/s before the arrival of the reflected shock. Another advantage of the fast-valve configuration is that it allows access to lower shock Mach numbers with a relatively steady core flow velocity prior to the arrival of the end wall reflected shock. As the shock Mach number is increased, a tendency for greater core flow acceleration is observed. As shown in Fig. 9a, the core flow acceleration in the fast-valve and single-diaphragm configurations is similar, indicating the valve can provide similar experimental conditions on average. The shot-to-shot variation in the fast-valve core velocity is about twice that in the burst disk data, however.

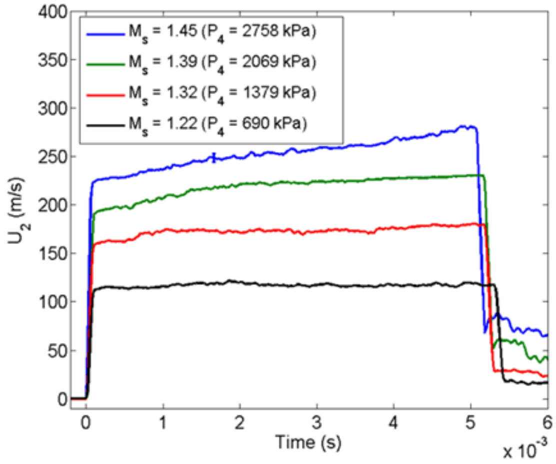

Fig. 10 Core flow velocity as a function of time using the fast-valve configuration at four different driver pressures.

Transient Wake Downstream of a Circular Cylinder

The transient wake growth downstream of the cylinder for an M_s = 1.32 experiment is shown in Fig. 11, where streamwise velocity contours are plotted along with overlaid velocity vectors. At this shock Mach number, the core flow velocity remains fairly steady over the roughly 5 ms of test time prior to the arrival of the end wall reflected shock (Fig. 10). The coordinate origin in the figure is defined to be at the trailing edge of the cylinder at the wall-normal center. At t = 36 µs (Fig. 11a), the incident shock has been slowed at the center of the vector field following its passage over the full-span cylinder. Two hundred µs later (Fig. 11b), two symmetrically oriented 'startup' vortices appear downstream of the cylinder centered at about y = -6 and y = 6 mm. The Stokes number for particles in these vortices is estimated to be about 0.5, which is probably at best, the upper limit for a particle to be expected to track the flow [22]. Inspection of PIV images showed particles within these startup vortices for this shock Mach number, but at a lower density than the surrounding flow. At higher shock Mach numbers (and therefore particle Stokes numbers), the seeding within the startup vortices was too low to return reliable correlations. Fortunately, as time continues during the transient wake growth, vortices become larger and velocity gradients become smaller, vastly improving the seed distribution. As time increases to 436 µs (Fig. 11c), the streamwise extent of the wake has grown as the initial pair of vortices has propagated and dissipated downstream. A second pair of symmetric vortices is observed just downstream of the cylinder. As time to progresses to 636 µs (Fig. 11d), the wake region has grown further in size and a third pair of vortices appears downstream of the cylinder. Inspection of the vector fields prior to this time showed that the third pair of vortices had an initially symmetric distribution similar to those at 436 µs. By 636 µs, however, the upper vortex is stronger as the wake has begun to exhibit some asymmetry. By 936 µs (Fig. 11e), the wake is beginning to oscillate in a periodic fashion consistent with von Kármán vortex shedding. In contrast, in the shock tube experiments of Asher and Dosanjh [17], only two symmetric vortex pairs formed prior to the wake going asymmetric. The von Kármán vortex shedding continues throughout the rest of the experiment until the arrival of the reflected shock. With continuing time, the oscillations grow to occupy nearly the entire vertical extent of the field-of-view (Fig. 11f, t = 4836 µs).

Since the pulse-burst PIV provides time series data, it is possible to perform spectral analysis at each vector field location. Along these lines, power spectral densities (PSDs) at x = 14 mm (x = d) and y = 0 are given in Fig. 12. The spectra were generated using the Welch windowing algorithm in the Mathworks software package (MatLab), where Blackman windows with an overlap of 50% were used. The spectra were calculated over a time interval that began after the incident shock left the field-of-view and ended just prior to the arrival of the reflected shock. Twenty separate experiments were averaged to produce the spectra, which had a frequency resolution of about 200 Hz. The streamwise PSD (Fig. 12a) contains a small peak with at a frequency f of 4860 Hz. In comparison, the wall-normal spectrum (Fig. 12b) has a much more prominent peak at 2430 Hz, which corresponds to the vortex shedding frequency. Thus, the peak in the streamwise PSD at 4860 Hz is a harmonic of the vortex shedding frequency. Taking the shock-induced velocity to be 175 m/s (Fig. 10) gives a Reynold number based on cylinder diameter Re_d of about 1.8 × 10^5. The Strouhal number of based on cylinder diameter ($S_t = fd/U_2$)

calculates to 0.19, a value consistent with the literature at this Re_d [30]. Another peak appears in the wall-normal spectrum corresponding to a second harmonic of the vortex shedding frequency.

In Fig. 12, the vortex shedding frequency appears prominently in the wall-normal PSD, but not in the streamwise PSD. To further explore this observation, the PSD value of each velocity component at the vortex shedding frequency is plotted over the entire vector domain in Fig. 13. This effectively plots the spatial distribution of velocity fluctuations at the vortex shedding frequency. The figure represents the average of twenty shock tube experiments. The streamwise spatial distribution (Fig. 13a) is near a minimum at $x = d$ and $y = 0$, which explains why a strong peak does not occur in the streamwise spectrum of Fig. 12a. On the other hand, just downstream of the cylinder, maximum PSD values occur in the streamwise distribution with locations centered at $y = 7$ and $y = -7$. These regions of large velocity fluctuations are explained by the oscillation of the separation point which occurs during vortex shedding. In contrast to the streamwise distribution, the distribution of wall-normal velocity fluctuations at the vortex shedding frequency exhibits a maximum at a location near $x = d$ and $y = 0$. The large wall-normal fluctuations at this location are associated with the vertical oscillations of the wake occurring in the von Kármán vortex street.

Although the preceding PSD discussion reveals quantitative information on vortex shedding using pulse-burst PIV, the PSDs do not yield information on the transient nature of the wake formation. To reveal such details, joint-time frequency analysis (JTFA) on the PIV data was conducted using a wavelet transform. This technique shows the frequency content of the disturbances as a function of time, and has been used in other unsteady applications such as wake transition, meteorological studies, and cavity flows [25-29]. The transform provides good time resolution. However, it has poor frequency resolution compared to alternate joint time-frequency methods such as the short-time-Fourier transform. The wavelet transform was computed using a Mathworks (Matlab) script provided in Ref. [29] using a Morelet mother wavelet.

The time evolution of the velocity fluctuations within the wake is shown in Fig. 14, where the amplitude of the wavelet transform is given as a function of time and frequency. The analysis was performed on velocity data from a single experiment (the same as that in Fig. 11) at locations where the vortex shedding frequency was most active. The JTFA for the streamwise velocity component (Fig. 14a) was performed at the location of $x = 3$ and $y = -6$. At this location, the most prominent frequency content occurs around the vortex shedding frequency of 2400 Hz. Following the passage of the shock at $t = 0$, it takes about 1 ms for the streamwise velocities associated with vortex shedding frequency to become active. It then takes another 1.5 ms to reach a peak value at about 2.5 ms. The vortex shedding activity then experiences a relative lull at 3.3 ms before once again gaining amplitude to reach a local maximum at 4.2 ms. These data correspond to a single shock tube experiment. Whether or not similar modulations of vortex shedding occur during other experiments will be investigated in future work.

The wall-normal JTFA (Fig. 14b) tell a similar story, though fluctuations associated with vortex shedding are greater in the wall-normal direction than in the streamwise direction, making the contour plot appear less noisy. The analysis was performed at the same location as the wall-normal PSD in Fig. 12. The wall-normal component of the wavelet transform begins to increase in amplitude at about 0.5 ms, which is about 0.5 ms earlier than in the streamwise direction. Like in the streamwise component, there is also modulation of the vortex shedding frequency, which results in a local minimum near 3.3 ms. In both the streamwise and wall-normal figures, the wavelet transform amplitude associated with vortex shedding reaches a minimum around 5.5 ms. The end wall reflected shock enters the field-of-view at about 5.2 ms (Fig. 10). Thus, it takes about 0.3 ms for the fluctuations associated vortex shedding to be dampened by the reflected shock.

The wavelet transform was also used to bandpass filter the velocity data about the vortex shedding frequency. This was achieved by setting wavelet transform coefficients other than those at the vortex shedding frequency to zero and then computing an inverse wavelet transform. This effectively bandpass filtered the velocity data without a time delay. The filter frequency bandwidth was approximately 200 Hz for this process.

The spatial distribution of streamwise velocity associated with the vortex shedding frequency is shown at four times in Fig. 15. The vector fields displayed are filtered versions of the instanteous velocity contours shown in Fig. 11. At $t = 236$ μs (Fig. 15a) and $t = 436$ μs (Fig. 15b) there is little frequency content at the von Kármán vortex shedding frequency, an observation consistent with the symmetric vortices shown in Fig. 11 at these times. On the other hand, there are large regions of positive and negative velocity just downstream of the cylinder at $t = 936$ μs (Fig. 15c). In comparison, at $t = 4836$ μs (Fig. 15d), the spatial distribution is inverted about $y = 0$ with a region of positive velocity appearing in the upper half of the vector field while a region of negative velocity appears in the lower half of the vector field. During the experiment, regions of positive and negative streamwise velocity enter the image field in an alternating fashion. A region of negative velocity just downstream of the cylinder is always followed in time by a region of positive velocity. The region of velocity vertically opposite always has the opposite sign. These observations are consistent with oscillatory boundary layer separation along the cylinder and the resultant vortex shedding.

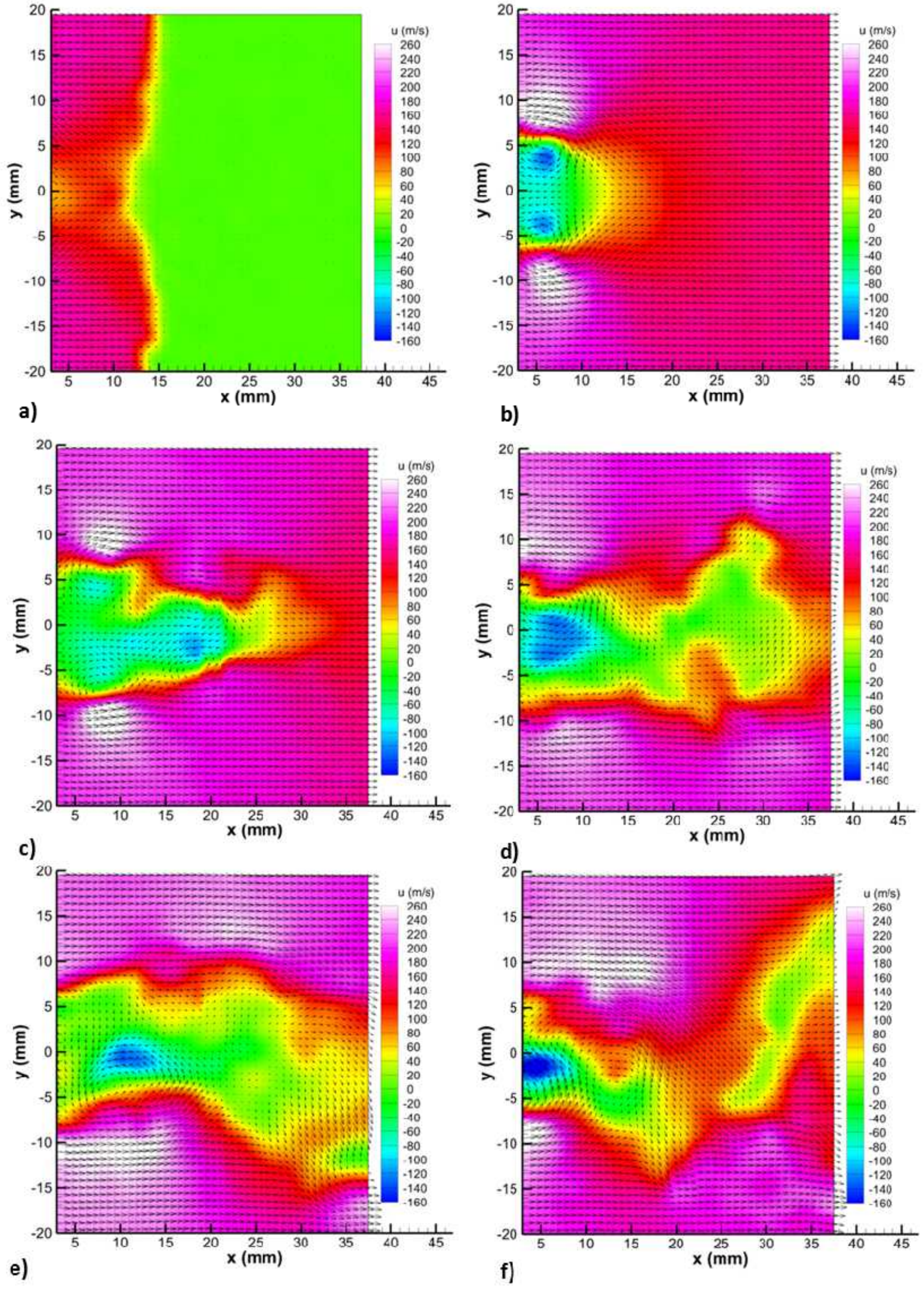

Fig. 11 Streamwise velocity contours and velocity vectors during a cylinder experiment with $M_s = 1.32$ at times: a) $t = 36$ μs, b) $t = 236$ μs, c) $t = 436$ μs, d) $t = 636$ μs, e) $t = 936$ μs, and f) $t = 4836$ μs.

Wall-normal velocities occurring at the vortex shedding frequency are displayed in Fig. 16. Similar to the streamwise velocities, the vertical velocities at the earlier times of 236 µs (Fig. 16a) and 436 µs (Fig. 16b) are small, an observation consistent with the temporal evolution of frequency content shown in Fig. 14b. Later, at t = 936 µs (Fig. 16c), a negative region of vertical velocity is just downstream of cylinder. Downstream of this appears a region of positive velocity centered at x = 22 mm, followed by another region of negative velocity centered at x = 42 mm. At t = 4836 µs (Fig. 16d), larger regions of negative and positive velocity appear in the figure as the vortex shedding has become more prominent. During an experiment, a region of positive vertical velocity always follows a region of negative velocity and vice-versa. Such a pattern is consistent with the large wall-normal flapping of the wake occurring during von Kármán vortex shedding.

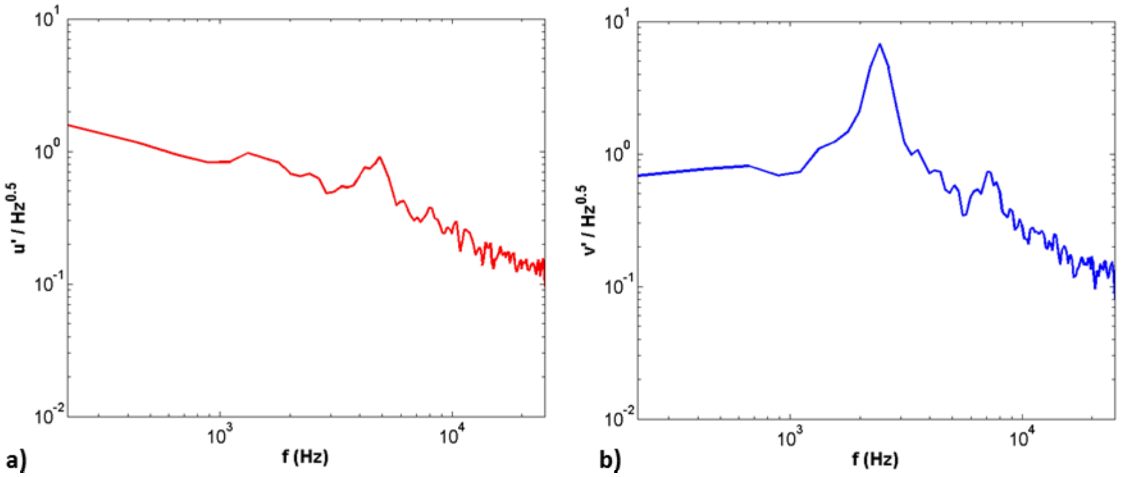

Fig. 12 Velocity PSDs one diameter downstream of the cylinder at y = 0: a) streamwise component, and b) wall-normal component.

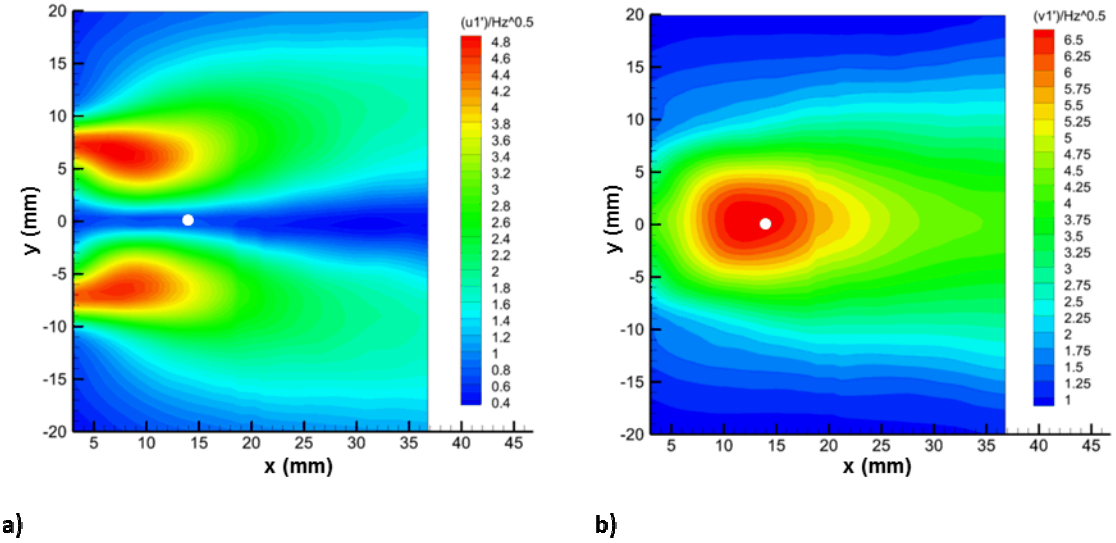

Fig. 13 Spatial distribution of the PSD amplitudes at the vortex shedding frequency of 2430 kHz: a) streamwise distribution, and b) wall-normal distribution. White dots are locations used for PSDs locations in the previous figure.

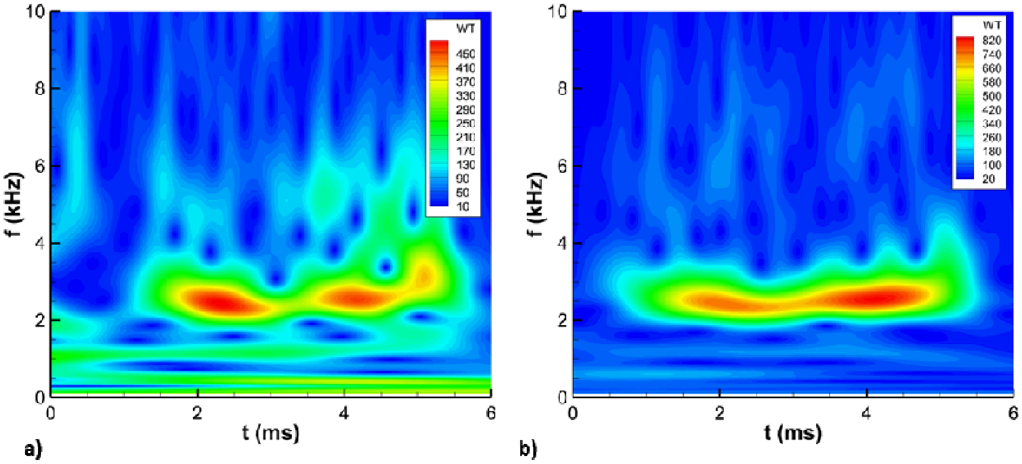

Fig. 14 JTFA: a) evolution of streamwise velocity content at *x* = 3 mm and *y* = -6 mm, and b) wall-normal frequency content at *x* = *D*, *y* = 0 (same as in Fig. 12b).

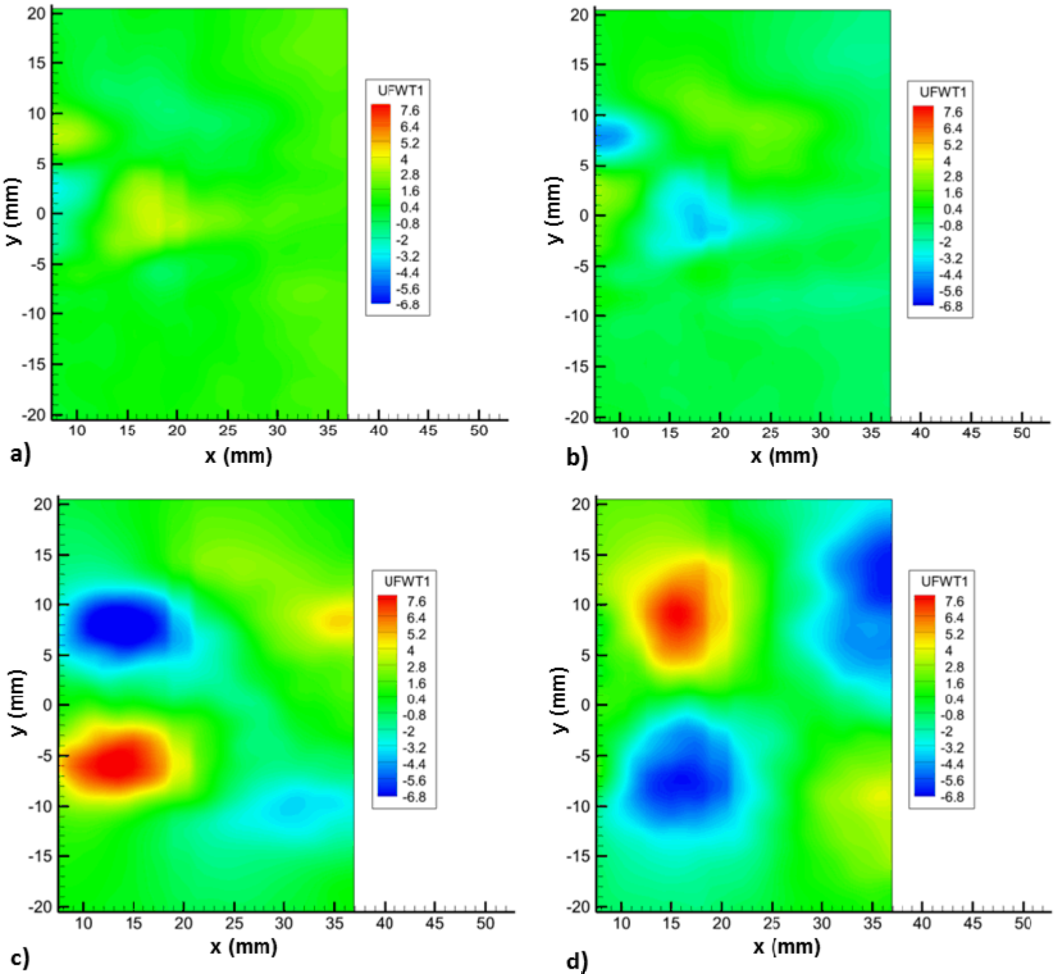

Fig. 15 Streamwise velocities (m/s) at the von Kármán vortex shedding frequency: a) *t* = 236 µs, b) *t* = 436 µs, c) *t* = 936 µs and d) *t* = 4836 µs.

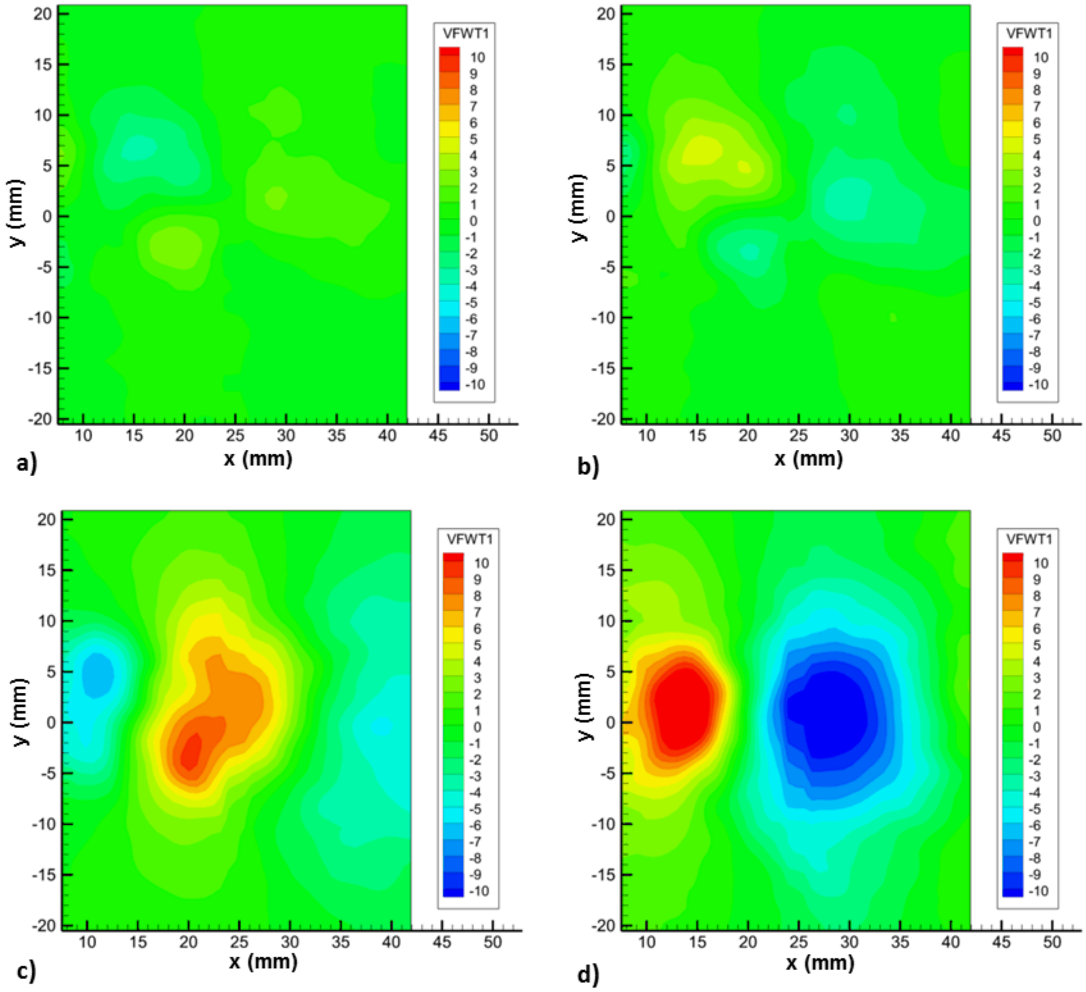

Fig. 16 Wall-normal velocities (m/s) at the von Kármán vortex shedding frequency: a) $t = 236$ μs, b) $t = 436$ μs, c) $t = 936$ μs and d) $t = 4836$ μs.

SUMMARY AND CONCLUSIONS

TR-PIV measurements were performed at a repetition rate of 50 kHz in a shock tube using a pulse-burst laser. In each experiment the driven section was initially air at atmospheric pressure and room temperature. Two transient flowfields were studied including the baseline flow in the empty shock tube and the wake growth downstream of a cylinder spanning the width of the test section.

The baseline experiments were conducted at incident shock Mach numbers ranging from 1.22 – 1.91. Turbulent boundary layer growth was observed following the passage of the incident shock in the baseline flow, while the core flow velocity increased with time. This measured core flow acceleration was compared to that predicted by the classical perturbation model of Mirels and Braun [7]. In some instances, the model did a good job predicting the core flow acceleration, though in others, the model under predicted the acceleration. Overall, the Mirels and Braun model can be considered a lower bound for predicting core flow acceleration in the MST. As a result of wall boundary layers, a significant amount of spatial non-uniformity remained in the flow following the passage of the end-wall reflected shock. The reflected shock did not slow the flow to zero velocity. The core flow velocity following the reflected shock increased with shock Mach number and test time (and wall boundary layer thickness).

In the impulsively started cylinder experiments, the wake downstream of the cylinder was symmetric immediately following the passage of the $M_s = 1.32$ incident shock. At later times, the wake transitioned to von a Kármán vortex street, following the shedding of three symmetric vortex pairs. The TR-PIV data were used to compute PSDs to investigate the frequency content in the wake. The PSDs showed peaks at the von Kármán vortex shedding frequency in both the streamwise and wall-normal velocity signals, although the spatial distribution of velocity fluctuations was found to be quite different for each velocity component. Harmonics of the vortex shedding frequency were also measured in the PSDs. JTFA was performed to quantify the frequency content of the wake flow as a function of time. The analysis showed that it took about 0.5 ms for the von Kármán vortex shedding frequency to become active at a location one diameter downstream of the cylinder at the wall-normal centerline. The velocity data were also bandpass filtered about the vortex shedding frequency to reveal spatial and temporal information. The bandpass filtered results showed a growth in wall-normal velocity fluctuations to occur as vortex shedding activity increased. In the streamwise bandpass filtered results, large regions of fluctuating velocity near the trailing edge of the cylinder were observed, which were consistent with an oscillating location of boundary layer separation.

ACKNOWLEDGEMENTS

Wavelet software was provided by C. Torrence and G. Compo , and is available at URL: http://paos.colorado.edu/research/wavelets/.

REFERENCES

[1] Balakumar BJ, Orlicz GC, Tompkins CD, Prestridge KP "Simultaneous particle-image velocimetry-planar laser-induced fluorescence measurements of Richtmyer-Meshkov instability growth in a gas curtain with and without reshock" Physics of Fluids 20 (2008).

[2] Beresh SJ, Kearney SP, Wagner JL, Guildenbecher DR, Henfling JF, Spillers RW, Pruett BO, Jiang, N, Slipchenko MN, Mance J, Roy S, "Pulse-Burst PIV in a High-Speed Wind Tunnel" Measurement Science and Technology 26 (2015).

[3] Mirels H "Shock Tube Test Time Limitation Due to Turbulent-Wall Boundary Layer" AIAA Journal 2 (1964).

[4] Mirels H "Flow Nonuniformity in Shock Tubes Operating at Maximum Test Times" Physics of Fluids 9 (1966).

[5] Mirels H "Attenuation in a Shock Tube Due to Unsteady-Boundary-Layer Action" National Advisory Committee for Aeronautics Report 1333 (1957).

[6] Trimpi RL and Cohen NB "A Theory for Predicting the Flow of Real Gases in Shock Tubes with Experimental Verification" National Advisory Committee for Aeronautics Technical Note, NACA TN-3375 (1955).

[7] Mirels H and Braun WH "Nonuniformities in Shock-Tube Flow Due to Unsteady-Boundary Layer Action" National Advisory Committee for Aeronautics Technical Note, NACA TN-4021 (1957).

[8] Igra O and Takayama K "Shock Tube Study of the Drag Coefficient of a Sphere in a Non-stationary Flow" Proceedings of the Royal Society of London 442 (1993).

[9] Devals C, Jourdan G, Estivalezes JL, Meshkov EE, and Houas L "Shock Tube Spherical Particle Accelerating Study for Drag Coefficient Determination" Shock Waves 12 (2003).

[10] Suzuki T, Sakamura Y, Igra O, Adachi T, Kobayashi S, Kotani A, and Funawatashi Y "Shock Tube Study of Particles' Motion Behind a Planar Shock Wave" Measurement Science and Technology 16 (2005).

[11] Jourdan G, Houas L, Igra O, Estivalezes JL, Devals C, and Meshkov EE, "Drag Coefficient of a Sphere in a Non-Stationary Flow: New Results," Proceedings of the Royal Society A 463 (2007).

[12] Wagner JL, Beresh SJ, Kearney SP, Pruett, BO and Wright EK "Shock tube investigation of quasi-steady drag in shock-particle interactions" Physics of Fluids 2 (2012).

[13] Taneda S "Visual study of unsteady separated flows around bodies" Progress in Aerospace Sciences 17 (1977).

[14] Chu CC and Liao YY "A quantitative study of the flow around an impulsively started circular cylinder" Experiments in fluids 13 (1992).

[15] Tonui N and Sumner D "Flow around impulsively started square prisms" Journal of Fluids and Structures, 27 (2011).

[16] Finaish F "On vortex structures and processes over bluff bodies in impulsive flow" Experiments in Fluids 11 (1991).

[17] Asher JA and Dosanjh DS "An Experimental Investigation of the Formation and Flow Characteristics of an Impulsively Generated Vortex Street" Journal of Fluids Engineering 90 (1968).

[18] Wagner JL, Beresh SJ, Kearney SP, Trott WM, Castaneda JN, Pruett BO, and Baer, MR "A multiphase shock tube for shock wave interactions with dense particle fields" Experiments in fluids 52 (2012).

[19] Slipchenko MN, Miller JD, Roy S, Gord JR., Danczyk SA, and Meyer TR "Quasi-Continuous Burst-Mode Laser for High-Speed Planar Imaging" Optics Letters 37 (2012).

[20] Slipchenko MN, Miller JD, Roy S, Gord JR and Meyer TR "All-Diode-Pumped Quasi-Continuous Burst-Mode Laser for Extended High-Speed Planar Imaging" Optics Express 21 (2013).

[21] Melling A "Tracer particles and seeding for particle image velocimetry" Measurement Science and Technology 8 (1997).

[22] Samimy M and Lele SK "Motion of Particles with Inertia in a Compressible Free Shear Layer" Physics of Fluids 3 (1991).

[23] Michael JV and Sutherland JW "The Thermodynamic State of the Hot Gas behind Reflected Shock Waves: Implication to Chemical Kinetics" International Journal of Chemical Kinetics 18 (1986).

[24] Masten A, Hanson RK, and Bowman CT "Shock Tube Study of the Reaction H + O2 → OH + O using OH Laser Absorption" Journal of Physical Chemistry 94 (1990).

[25] Kegerise MA, Spina EF, Garg S, Cattafesta LN “Mode-Switching and Nonlinear Effects in Compressible Flow Over a Cavity,” Physics of Fluids 16 (2005).

[26] Wagner JL, Casper KM, Beresh SJ, Arunajatesan S, Henfling JF, Spillers RW, and Pruett, BO “Relationship between Acoustic Tones and Flow Structure in Transonic Cavity Flow” Presented at the 45th AIAA Fluid Dynamics Conference (2015).

[27] Shaikh FN and Gaster M “The Non-Linear Evolution of Modulated Waves in a Boundary Layer” Journal of Engineering Mathematics 28 (1994).

[28] Jordan D, Miksad RW, and Powers EJ “Implementation of the Continuous Wavelet Transform for Digital Time Series Analysis,” Review of Scientific Instruments 68 (1997).

[29] Torrence C and Compo GP “A Practical Guide to Wavelet Analysis” Bulletin of the American Meteorological Society 79 (1998).

[30] Roshko A "Experiments on the flow past a circular cylinder at very high Reynolds number" Journal of Fluid Mechanics 10 (1961).